

RESEARCH ARTICLE | APRIL 01 2025

Machine-learning potential energy surfaces implications in photodissociation process FREE

Special Collection: **Advances in Mathematics and Physics: from Complexity to Machine Learning**Joaquin de la Cerdá  ; Johan F. Triana   Check for updates

Chaos 35, 043102 (2025)

<https://doi.org/10.1063/5.0249690>

Articles You May Be Interested In

Selective bond breaking mediated by state specific vibrational excitation in model HOD molecule through optimized femtosecond IR pulse: A simulated annealing based approach

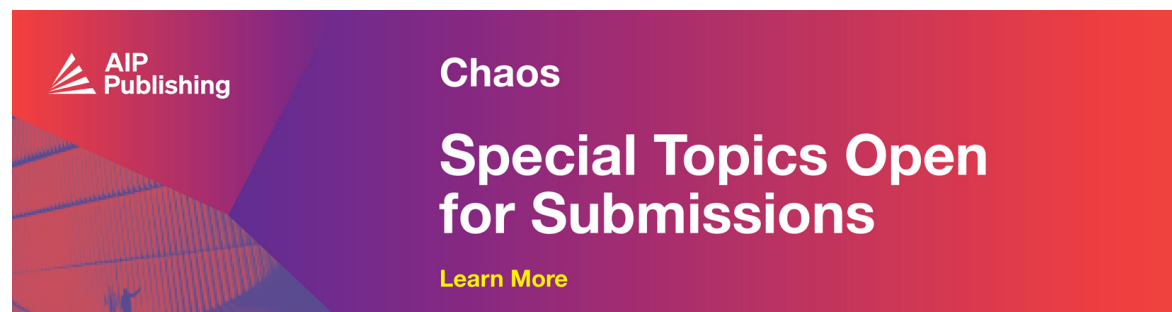
J. Chem. Phys. (July 2013)

Selective photodissociation of O–H and O–D bonds from ground vibrational state of HOD using simple UV pulses

J. Chem. Phys. (July 2007)

Deep learning-based image Steganalysis

AIP Conf. Proc. (September 2024)



Machine-learning potential energy surfaces implications in photodissociation process

Cite as: Chaos 35, 043102 (2025); doi: 10.1063/5.0249690

Submitted: 19 November 2024 · Accepted: 19 March 2025 ·

Published Online: 1 April 2025



View Online



Export Citation



CrossMark

Joaquin de la Cerda  and Johan F. Triana 

AFFILIATIONS

Department of Physics, Universidad Católica del Norte, Av. Angamos 0610, Antofagasta, Chile

Note: This paper is part of the Special Topic on Advances in Mathematics and Physics: from Complexity to Machine Learning.

^{a)}**Author to whom correspondence should be addressed:** johan.triana@ucn.cl

ABSTRACT

Multi-state quantum molecular dynamics is one of the most accurate methodologies for predicting rates and yields of different chemical reactions. However, the generation of potential energy surfaces (PES), transition dipoles, and non-adiabatic couplings from *ab initio* calculations become a challenge, especially because of the exponential growth of computational cost as the number of electrons and molecular modes increases. Thus, machine learning (ML) emerges as a novel technique to compute molecular properties using fewer resources. Yet, the validity of ML methodologies continues in constant development, particularly for high-energy regions where conventional *ab initio* sampling is reduced. We test the accuracy of the potential energy surfaces interpolated with machine learning (ML) techniques in the solution of the time-dependent Schrödinger equation for the conventional IR+UV bond-breaking process of semi-heavy water. We perform a statistical analysis of the differences in expectation values and dissociation probabilities, which depend on the number of *ab initio* points selected to generate the machine learning potential energy surface (ML-PES). The energy differences of the electronic excited state modify population transfer from the ground state by driving with a UV laser pulse. We consider as the exact solution the photodynamics implemented with analytical expressions of the electronic ground $\tilde{\chi}^1A_1$ and excited $\tilde{\chi}^1B_1$ states. The results of the mean bond distance and dissociation probabilities suggest that ML-PES is suitable for dynamics calculations around the Franck–Condon region, and that standard interpolation methods are more efficient for multistate dynamics that involve dissociative and repulsive energy regions of the electronic states. Our work contributes to the continued inclusion of ML tools in molecular dynamics to obtain accurate predictions of dissociation yields with fewer computational resources and non-written rules to follow in multi-state dynamics calculations.

Published under an exclusive license by AIP Publishing. <https://doi.org/10.1063/5.0249690>

One of the biggest challenges to perform quantum molecular dynamics is the potential energy surface (PES), which requires huge computational resources as the number of electrons and nuclear degrees of freedom increase. Hence, machine-learning techniques arise as a methodology to interpolate or predict energies and transition dipoles to reduce computational costs. We test the accuracy of the ML-PES in the IR+UV photodynamics of the semi-heavy water molecule that leads to dissociation in H+OD and D+OH channels. The mechanism involves a multidimensional molecular dynamics simulation in two electronic states, which requires at least 2000 *ab initio* data points, which for heavier molecules can be computationally expensive. As part of our results, we detect that ML techniques work properly for dynamics simulations around the molecular equilibrium region, in contrast to mechanisms that involve dissociative and repulsive

energy regions. Our work represents a significant contribution to the growing field of molecular dynamics aided by ML techniques.

I. INTRODUCTION

Theoretical principles of multidimensional molecular dynamics provide tools to describe many phenomena in physics and chemistry. Many unresolved issues remain in chemical physics, particularly in determining an accurate *ab initio* potential energy surface (PES) that allows the study of all chemical processes of a determined molecule. Combined methodologies between *ab initio* calculations with conventional fitting processes can produce PES with great accuracy.^{1–5} However, the generation of analytical expressions to represent one potential energy surface with three degrees of

freedom can lead to complex expressions.¹ Other methodologies like molecular dynamics simulations on the fly compute the region of PESs that wavepacket crosses, which reduces the number of *ab initio* energy points needed to perform dynamics calculations and computational resources, but the accuracy goal begins to be a challenge.⁶⁻⁸ Thus, new interpolating and predicting methodologies are required as tools to simplify *ab initio* calculations and reduce computational costs.

Machine Learning (ML) emerges as a novel concept to compute additional energy points and dipole moments based on its adaptability to learn patterns from *ab initio* data points,⁹⁻¹¹ which has been for a long time the cornerstone in computational theoretical chemistry¹¹ and non-linear dynamics.¹² The majority of ML techniques have been applied to study chemical properties and processes at the ground electronic state level.¹³⁻¹⁶ For example, to predict the rovibrational molecular spectroscopic properties under an isotopic substitution of systems with noble gases for astrophysical interests¹⁷ and to reduce the error between the theory and experiment in comparison with hybrid DFT approaches.¹⁸ In addition, previous studies involving electronic excited states implement ML methodologies to calculate additional points of transition dipole moments,¹⁹ non-adiabatic couplings,²⁰ to study non-adiabatic dynamics around conical intersections,²¹⁻²³ the generation of adiabatic machine learning potential energy surfaces for studying reaction probabilities,²⁴ and applications of machine learning techniques for excited states based on time-dependent density functional theory calculations.²⁵ Some works hybridize ML techniques with on-the-fly calculations to accelerate nonadiabatic molecular dynamics,²² others implement the Kernel ridge regression method to generate accurate dipole moment functions for the isomerization dynamics of the azomethane inside a Fabry-Pérot cavity,²⁶ which is of great importance in cavity quantum electrodynamics simulations.^{27,28} In the context of branching ratios prediction, ML-PES have been implemented for gas-phase and gas-surface scattering processes²⁹ and for benchmarking quantum scattering in collision systems with helium atoms, where the number of *ab initio* points makes conventional spline interpolation inefficient.³⁰ These studies at the excited electronic state level obtain remarkable accuracy in comparison with on-the-fly molecular dynamics. However, studies of the chemical product yield and dissociation probability accuracy with ML-PES are still scarce, and comparisons with complete *ab initio* calculations are required to know the scope of ML techniques under different mechanisms, such as laser pulse excitations in high-energy regions of the potential energy surfaces.

The use of ultrashort laser pulses to gain active control in the yields of photoinduced chemical reactions is nowadays a well-established research topic. In spite of the great advances in *ab initio* theoretical and computational procedures, the prediction of the branching ratios of photofragmentation channels is still a challenging task, even in the case of simple molecules. In this work, the photofragmentation dynamics of HOD molecule is revisited as an example to find the statistical implications for carrying out photodynamics calculations with machine learning potential energy surfaces (ML-PESs) computed with small datasets, which are also compared with fitted PESs by implementing a 2D spline interpolation with the smallest dataset. We study the IR+UV pump-dump control scheme to drive the molecular system to selective bond

breaking,^{31,32} where forces in the excited electronic state are not bond-selective due to symmetry. The use of a pump-IR pulse prior to a UV pulse with a controlled delay becomes crucial to produce a selective bond breaking. We validate the accuracy of implementing ML-PES in photodissociation processes with reduced datasets that consider the conventional sampling of *ab initio* calculations for a complete potential energy surface, where the grid points are reduced in the repulsive and dissociative regions in comparison with points around the Franck-Condon region. The results are analyzed statistically via expectation values and dissociation probabilities in the electronic ground and excited state, respectively.

The efficiency of ML methods in high-energy or pulse laser excitation processes could improve the understanding of the greenhouse effect by studying carbon dioxide photodissociation³³ and bond-breaking mechanisms in interstellar environments.³⁴ Due to the presence of different chemical reactions that occur in the open air beyond the stratosphere, it becomes significant.

The article is organized as follows: in Sec. II, we describe the semi-classical light-matter interaction Hamiltonian to compute the IR+UV photodynamics of the HOD molecule and the process to calculate the machine-learning potential energy surfaces (ML-PESs) from different datasets. In Sec. III, we compute the ground state energy, the mean bond distance, and dissociation probabilities by using the machine learning potential energy surfaces found in Sec. II. We also discuss the statistical implications of implementing potential energy surfaces interpolated with machine learning techniques with small datasets. Finally, we conclude our findings in Sec. IV.

II. METHODOLOGY

A. Hamiltonian model for dissociation control of semi-heavy water molecule (HOD)

We model the semi-heavy water molecule considering that the molecule is in the *xy*-plane, the bond angle is fixed to its equilibrium value $\gamma = 104.5^\circ$, and the oxygen atom is the origin, which reduces the nuclear Hamiltonian to only two radial degrees of freedom, R_H and R_D . These two internal coordinates describe the bond distances OH and OD, respectively. The semi-classical light-matter Hamiltonian is given by

$$\hat{H} = \hat{H}_M - \vec{d}(R_H, R_D) \cdot \vec{E}(t), \quad (1)$$

where the molecular Hamiltonian \hat{H}_M is represented in two electronic states ($\tilde{X}^1A_1, \tilde{A}^1B_1$) and interacts with the electric laser pulses $\vec{E}(t)$ via transition dipole moment $\vec{d}(R_H, R_D)$. \hat{H}_M can be expressed in the form

$$\begin{aligned} \hat{H}_M = & \left[-\frac{1}{2\mu_D} \frac{\partial^2}{\partial R_D^2} - \frac{1}{2\mu_H} \frac{\partial^2}{\partial R_H^2} - \cos\theta \frac{1}{M_O} \frac{\partial^2}{\partial R_D \partial R_H} \right] \cdot \mathbb{1} \\ & + \begin{pmatrix} \hat{V}_G & 0 \\ 0 & \hat{V}_E \end{pmatrix}, \end{aligned} \quad (2)$$

where μ_i are the reduced masses, M_O is the oxygen mass, and \vec{V}_i are the potential energy surfaces of the ground (\tilde{X}^1A_1) and excited (\tilde{A}^1B_1) electronic states. The semi-classical interaction Hamiltonian

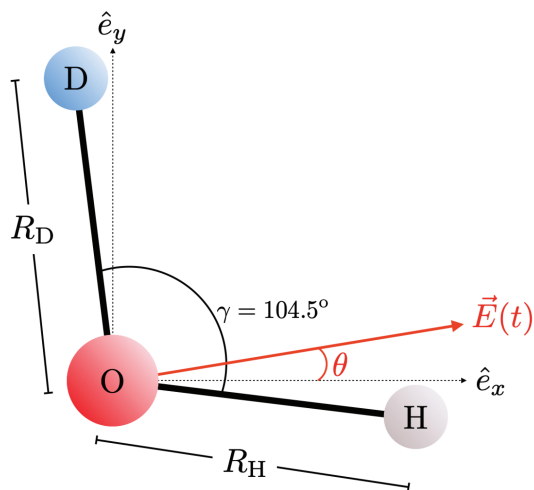


FIG. 1. Position of the semi-heavy water molecule in space. The HOD molecule is in the xy -plane with the oxygen atom in the origin of coordinates. Hydrogen and deuterium atoms form an angle of 7.5° with the x -axis and y -axis, respectively. The red line represents the electric field $\vec{E}(t)$ at a polarization angle θ .

with laser pulses is given by

$$\vec{d}(R_H, R_D) \cdot \vec{E}(t) = \begin{pmatrix} \vec{d}_{gg} \cdot \vec{E}_{IR}(t) & \vec{d}_{ge} \cdot \vec{E}_{UV}(t) \\ \vec{d}_{ge} \cdot \vec{E}_{UV}(t) & 0 \end{pmatrix}, \quad (3)$$

where the permanent dipole moment \vec{d}_{gg} for the electronic ground state is expressed as a superposition of two Mecke-type dipole functions for the OH and OD bonds given by

$$\begin{aligned} \vec{d}_{gg}(R_H, R_D) &= \left[\cos\left(\frac{\gamma - 90^\circ}{2}\right) d_g(R_H) - \sin\left(\frac{\gamma - 90^\circ}{2}\right) d_g(R_D) \right] \\ &\quad \times \hat{e}_x - \left[\sin\left(\frac{\gamma - 90^\circ}{2}\right) d_g(R_H) + \cos\left(\frac{\gamma - 90^\circ}{2}\right) d_g(R_D) \right] \hat{e}_y, \end{aligned} \quad (4)$$

where each Mecke-type dipole function is $d_g(R_i) = d_0 R_i e^{-R_i/R_0}$, with $d_0 = 4.15 \text{ Debye}/a_0$ and $R_0 = 1.134 a_0$ for the equilibrium bond angle γ and HOD molecule oriented as in Fig. 1, where a_0 is the Bohr radius. The model of transition dipole moment \vec{d}_{ge} that connects the two electronic states was proposed in Ref. 2, and it can be written as

$$\vec{d}_{ge}(R_H, R_D) = \frac{B}{(1 + e^{R_H - R_{eq}})(1 + e^{R_D - R_{eq}})} \hat{e}_z, \quad (5)$$

with $B = 12.58 \text{ Debye}$ and $R_{eq} = 1.81 a_0$. All the effects due to the intra-state dipole moment of the excited state are neglected ($\vec{d}_{ee} = 0$).

The mechanism for selective bond breaking considers a superposition of two electric field pulses, $\vec{E}_{IR}(t)$ interacts with the electronic ground state with a carrier frequency at the infrared regime and $\vec{E}_{UV}(t)$ is an ultrashort laser pulse with a carrier frequency in the

ultraviolet regime, which is delayed respect to $\vec{E}_{IR}(t)$. We consider the pulses are linearly polarized along unit vector \hat{e}_k . Thus, the total electric field $\vec{E}(t)$ can be written in general form as

$$\vec{E}(t) = E_{IR}(t)(\cos \theta \hat{e}_x + \sin \theta \hat{e}_y) + E_{UV}(t) \hat{e}_z, \quad (6)$$

with

$$\begin{aligned} E_k &= \Theta(t - \tau_k - T_k/2) E_{0k} \sin^2 \left[\frac{\pi}{T_k} (t - \tau_k + T_k/2) \right] \\ &\quad \times \sin[\omega_k(t - \tau_k + T_k/2)] \Theta(\tau_k + T_k/2 - t), \end{aligned} \quad (7)$$

where θ is the polarization angle, τ_k is the time delay, T_k is the pulse duration, $\omega_k = \{\omega_{IR}, \omega_{UV}\}$ is the frequency of the laser, and $\Theta(t)$ are Heaviside functions. The pulse parameters implemented are given in Table I.

B. Machine learning potential energy surfaces

1. \tilde{X}^1A_1 ground state

The \tilde{X}^1A_1 PES is parametrized by Morse potentials with a coupling term between the bond length coordinates given by²

$$V_G(R_H, R_D) = D \left[1 - e^{-\beta(R_H - R_0)} \right]^2 + D \left[1 - e^{-\beta(R_D - R_0)} \right]^2 - \frac{A(R_H - R_0)(R_D - R_0)}{1 + e^{[(R_H - R_0) + (R_D - R_0)]}}, \quad (8)$$

where $D = 5.692 \text{ eV}$, $\beta = 1.1327/a_0$, $R_0 = 1.81 a_0$, and $A = 1.84 \text{ eV}/a_0^2$. Since our goal is to determine differences in dissociation probability by solving the time-dependent Schrödinger equation with a complete *ab initio* potential energy surface (PES) and interpolated machine learning potential energy surfaces (ML-PESs), we generate three different datasets from Eq. (8), which are training for building the corresponding ML-PES.

Datasets are calculated by setting R_H and R_D in the interval $0.8a_0 < R_k < 6.0a_0$. We consider in dataset A 21 grid points per coordinate, which leads to 441 energy points, dataset B has 32 grid points in each coordinate giving rise to 1024 energy points, and dataset C with 43 grid points per coordinate for 1849 configurations. The corresponding grid points can be found in Appendix A. The learnable hyperparameters required to obtain the highest accurate ML-PES are found by implementing the Keras-Tuner library,³⁵ which optimizes the hyperparameters of the Neural Network (NN) within a model composed of seven hidden layers that minimizes the loss function that characterizes the error. We implement the hyperband Keras-Tuner optimization method for each dataset to obtain its own set of hyperparameters that gives the highest accurate ML-PES by splitting the data in a 80/20 ratio, equivalent to a 20% of points for validation. We consider that each layer can have a maximum of 512 neurons, Keras-Tuner chooses the activation function between relu, tanh, and sigmoid for each layer, and the learning rate interval from 0.0001 to 0.01. Furthermore, the maximum number of epochs is 2000. The optimal hyperparameters resulting from the ML models with seven layers of each dataset are given in Table II.

We point out that after several tests varying the number of layers, epochs, and neurons, the optimal number of layers is seven,

TABLE I. Laser pulse parameters. Time delays τ_k , pulse time duration T_k , electric field amplitude E_{0k} , electric field polarization θ , and carrier frequencies ω_k for IR and UV laser pulses to control dissociation of H+OD (mode R_H) and D+OH (mode R_D) channels.

Mode	Infrared					UV		
	τ_{IR} (fs)	T_{IR} (fs)	$E_{0\text{IR}}$ (a.u.)	ω_{IR} (eV)	θ	τ_{UV} (fs)	T_{UV} (fs)	$E_{0\text{UV}}$ (a.u.)
R_H	40.0	50.0	0.1	0.46	0.0	59.0	3.0	0.05
R_D	40.0	50.0	0.1	0.34	0.5π	65.5	3.0	0.05

and more than 512 neurons per layer increase in the complexity of the ML model, which could lead to overfitting. The quality of the resulting ML-PES is validated by monitoring the mean absolute percentage error (MAPE), which is calculated as $\text{MAPE} = (100/N) \sum_{i=1}^N |V^{(k)}(\mathbf{Q}_i)/V_G(\mathbf{Q}_i) - 1|$, where $V^{(k)}(\mathbf{Q}_i)$ are the predicted energies by ML model $k = \{A, B, C\}$ for coordinate configuration \mathbf{Q}_i and reference energies $V_G(\mathbf{Q}_i)$ [Eq. (8)]. N is the total number of energy points and depends on each dataset.

Figures 2(a)–2(c) show the comparison of the ground electronic state \tilde{X}^1A_1 for the different predictions with the exact potential energy surface in Eq. (8). It is possible to visualize that at the equilibrium point ($R_H = R_D = 1.81a_0$), there is a minimum and in dissociation regions ($R_H = R_D \sim 5.0a_0$), there is a plate as it is expected for a PES of two coupled Morse potentials. Figure 2(a) compares ML-PES calculated from dataset A with the exact PES from Eq. (8), where we observe notorious differences in almost all regions except at equilibrium positions. The validation gives a mean absolute percentage error (MAPE) of 1.16%. For dataset B and C in Figs. 2(b) and 2(c), respectively, the differences can be neglected, which is supported by the $\text{MAPE}^{(B)} = 0.65\%$ and $\text{MAPE}^{(C)} = 0.73\%$. Note that most of the differences with the exact PES are presented in the dissociative and repulsive energy regions, which correspond to the energy points with the highest values. These points are illustrated by blue-shaded regions in Figs. 2(a)–2(f), where the errors are more notorious [see, e.g., Fig. 2(d)]. Hence, it is expected that dynamics calculations along the ML-PES that do not involve high-energy regions in the \tilde{X}^1A_1 electronic state obtain small errors.

Figures 2(d)–2(f) show the correlation plots for the performance of the ML-PES against the reference energy points for validation

data of each dataset. It is worth mentioning that $\text{MAPE}^{(C)} > \text{MAPE}^{(B)}$ because of the difference of predicted high energy points in the repulsive region ($R_H = R_D \sim 1.2a_0$). However, these specific high-energy points are irrelevant for the purpose of this work due to wave packet evolution does not cross over that region.

2. \tilde{A}^1B_1 excited state

The \tilde{A}^1B_1 PES was parametrized by Engel¹ in terms of the distance between the atoms of the water molecule, i.e., the two bond lengths R_H and the distance between hydrogen atoms R_{HH} . Because the potential energy surfaces depend on the number of electrons of the molecule, PESs for H_2O are equivalent for the semi-heavy water molecule HOD. Hence, we consider that the excited electronic state is given in terms of the bond lengths R_H and R_D , and the distance between the hydrogen and deuterium atoms R_{HD} . Thus, the electronic excited state is fitted to the analytic expression

$$V_E(R_H, R_{HD}, R_D) = V_{OH}(R_H)\chi(R_{HD}, R_H) + V_{OH}(R_D)\chi(R_H, R_{HD}) + V_I(R_H, R_{HD}, R_D), \quad (9)$$

where $V_{OH}(R_k)$ is a Morse potential for coordinate R_k , $\chi(R_i, R_j) = (1 - e^{-\delta R_i^2})(1 - e^{-\delta R_j^2})$ are cutoff functions, and V_I is the interaction function given by

$$V_I(R_H, R_{HD}, R_D) = \sum_{i=1}^{50} c_i P_i(S_H, S_{HD}, S_D) \prod_{j=1}^3 (1 - \tanh \alpha_j S_j), \quad (10)$$

TABLE II. ML-PES hyperparameters for \tilde{X}^1A_1 and \tilde{A}^1B_1 electronic states found by Keras-Tuner. Number of neurons N , activation functions, and learning rate implemented in the training model composed of seven hidden layers for datasets A, B, and C.

DS	Layer 1		Layer 2		Layer 3		Layer 4		Layer 5		Layer 6		Layer 7		L. rate
	N	Act. func.													
\tilde{X}^1A_1 Electronic ground state															
A	62	tanh	209	tanh	123	relu	458	relu	349	tanh	489	relu	45	sigmoid	2.46×10^{-4}
B	403	relu	505	tanh	263	relu	402	tanh	371	tanh	398	relu	15	sigmoid	2.19×10^{-4}
C	403	relu	505	tanh	263	relu	402	tanh	371	tanh	398	relu	15	sigmoid	2.19×10^{-4}
\tilde{A}^1B_1 Electronic excited state															
A	98	tanh	149	tanh	282	tanh	416	relu	479	relu	162	relu	265	tanh	2.46×10^{-4}
B	479	relu	110	sigmoid	241	tanh	367	tanh	472	sigmoid	397	relu	424	relu	8.95×10^{-4}
C	470	relu	410	tanh	298	sigmoid	230	relu	324	sigmoid	500	relu	408	relu	8.41×10^{-4}

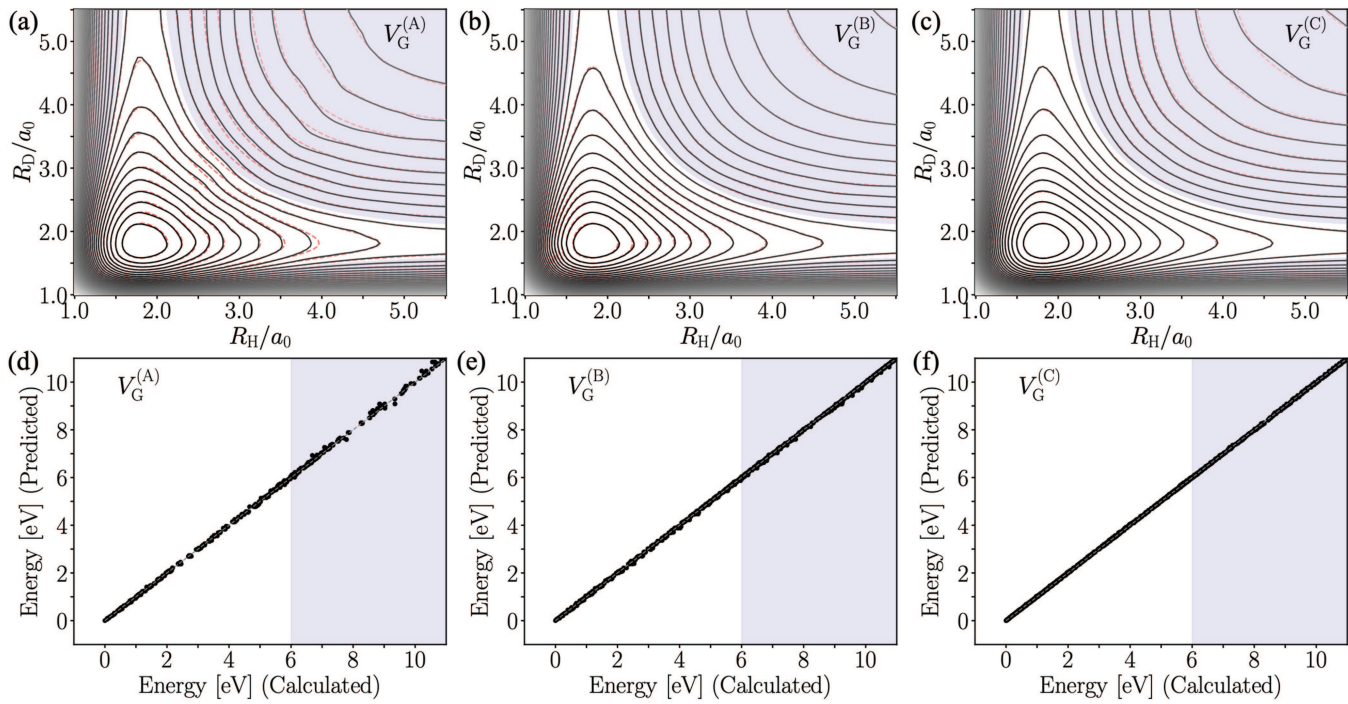


FIG. 2. ML-PES for the ground state \tilde{X}^1A_1 . (a)–(c) Contour plots of the ML-PES (solid lines) compared with exact PES given in Eq. (8) (red-dashed contour) for datasets A, B, and C. (d)–(f) Correlation plots for the ML-PES against exact energies for the same datasets used in (a)–(c). The energy points inside the shaded region correspond to the energy region highlighted in (a)–(c).

where P_i is a polynomial up to six orders in all variables with $S_j = r_j - 1 \text{ \AA}$. The necessary parameters to produce the first excited state of HOD are found in Ref. 1. Electronic state \tilde{A}^1B_1 in Eq. (9) is transformed to coordinates R_H and R_D by a cosine law of the form $R_{\text{HD}}^2 = R_H^2 + R_D^2 - 2R_H R_D \cos \theta$, with $\theta = 104.5^\circ$.

Following the procedure performed for the \tilde{X}^1A_1 electronic ground state in Sec. II B 1, we also train three different datasets of energy points from Eq. (9) as *ab initio* points calculated. We consider the same intervals for coordinates R_H and R_D and, therefore, equal number of energy points for each dataset. The learnable optimized hyperparameters required to obtain the highest accurate ML-PES are found by implementing the hyperband Keras-Tuner optimization method in the electronic excited state V_E . ML hyperparameters for all datasets of the \tilde{A}^1B_1 electronic state are given in Table II.

Figures 3(a)–3(c) show the comparison of the electronic state \tilde{A}^1B_1 for the different predictions with the exact potential energy surface in Eq. (9), where at the point $(R_H, R_D) = (2.3a_0, 2.3a_0)$, a saddle point is located. The localization of a saddle point along the bisection $R_H = R_D$ and the symmetry of the potential makes this state a non-bond selective potential. As in the case of the electronic ground state, Fig. 3(a) compares ML-PES calculated from dataset A with the exact PES, where we observe notorious differences in all regions of the potential energy surface. The validation gives a

mean absolute percentage error of 3.03%. Dataset B in Fig. 3(b) also shows notorious differences with a $\text{MAPE}^{(B)} = 2.69\%$. In the case of dataset C, differences are presented only in the dissociative ($R_H = R_D > 3.0a_0$) and repulsive ($R_H = R_D < 1.4a_0$) energy regions [see the shaded region in Fig. 3(c)]. In this case, the mean absolute percentage error has a value of $\text{MAPE}^{(C)} = 1.62\%$. Similar to the ML-PES of the ground state, most of the differences belong to high-energy regions for dataset C. Hence, minimum differences in photodynamics calculations are expected from the results with ML-PES with dataset C. Figures 3(d)–3(f) show the correlation plots for the performance of the ML-PES against the reference energy points $V_E(Q)$ for validation data of each dataset.

We point out that this electronic excited state is a dissociative potential, which makes it highly non-linear, as the expansion in Eq. (10) demonstrated. Hence, ML training models with MAPE values lower than $\text{MAPE}^{(C)}$ for \tilde{A}^1B_1 electronic potential could be hard and computationally expensive to obtain because of the reduced number of data points in the dissociative ($R_H = R_D \gtrsim 3.5$) and returning point ($R_H = R_D \lesssim 1.5$) energy regions. We remark that there is a non-existent theory that guarantees these very small errors in complex potentials, and that our work focuses on the effects of a ML-PES in photodissociation processes. ML training models with a high complexity for the electronic excited state are out of the scope of this work.

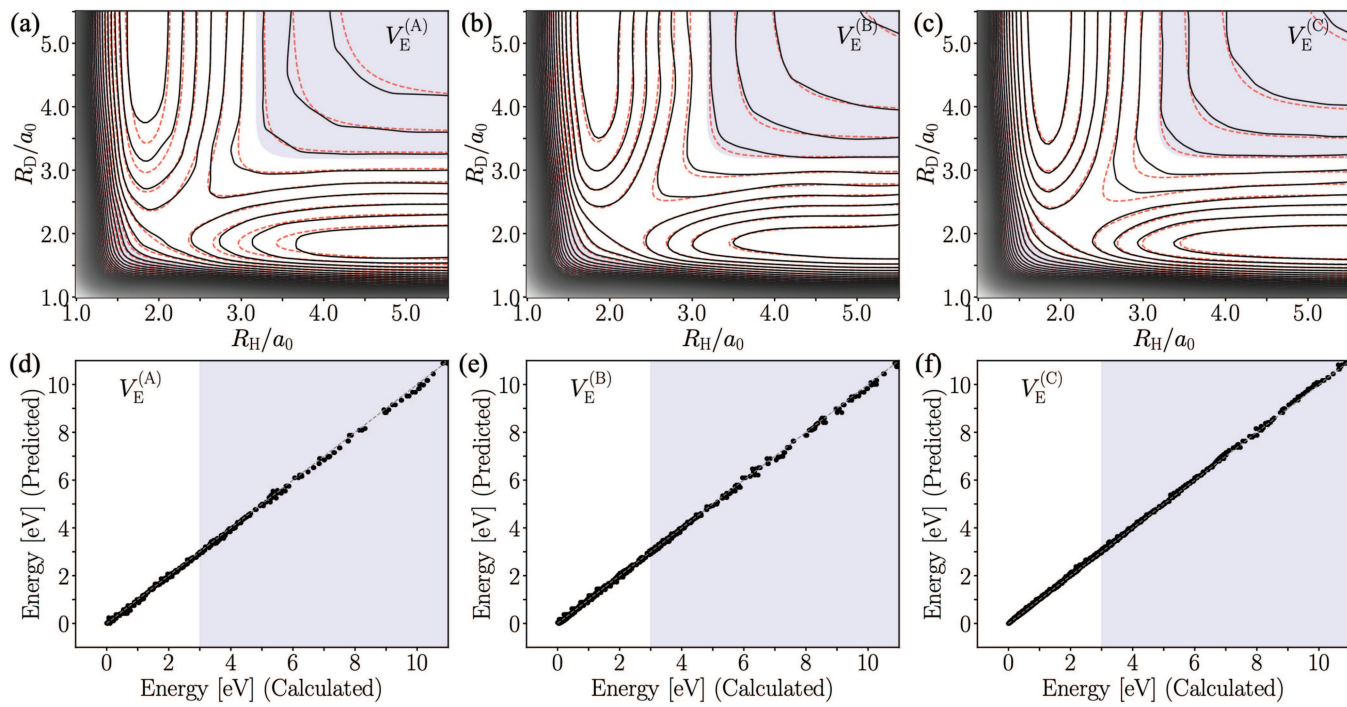


FIG. 3. ML-PES for the excited state \tilde{A}^1B_1 . (a)–(c) Contour plots of the ML-PES (solid lines) compared with exact excited PES given in Eq. (9) (red-dashed contour) for datasets A, B, and C. (d)–(f) Correlation plots for the ML-PES against exact energies for the same datasets used in (a)–(c). The energy points inside the shaded region correspond to the energy region highlighted in (a)–(c).

C. Dissociative dynamics for HOD

Control of the dissociation rates for the HOD molecule depends on the duration time, driving frequency of IR and UV laser pulses, and the time delay between these two pulses. The route of the mechanism initializes in the vibrational ground state of the electronic ground state \tilde{X}^1A_1 , which is excited by an IR laser pulse to generate excitations in the normal or local modes. Then, followed by a subsequent excitation to the electronic excited state \tilde{A}^1B_1 by a second UV laser pulse, where the reduced mass asymmetry between OH and OD stretching modes generates a higher selection probability for the lighter mode, corresponding to the OH bond. In a sudden photoexcitation, the ground vibrational state of \tilde{X}^1A_1 is excited to the \tilde{A}^1B_1 state, and the newly created wavepacket sits on the bisection line and a major portion of the wavepacket dissociates along the R_H coordinate and the remaining part along the R_D one because of the reduced mass difference. Note that in this model, the molecular rotation is neglected, and the bending mode is frozen due to the time scales of nuclear dynamics (~ 100 – 200 fs) being much faster than time scales of rotational effects (~ 2 – 3 ps).

For accurately calculating the bond-breaking probability of OH or OD molecular bonds of semi-heavy water following the mechanism described above, we solve the time-dependent Schrödinger equation in coordinate space with a Hamiltonian given by Eq. (1) implementing the multi-configuration time-dependent Hartree (MCTDH) method.^{36–38} The MCTDH wave function ansatz for

internal coordinates R_H and R_D in the *multi-set* formulation can be written as

$$\Psi(R_H, R_D, t) = \sum_{\alpha=1}^2 \sum_{j_H=1}^{n_H} \sum_{j_D=1}^{n_D} A_{j_H j_D}(t) \phi_{j_H}^{(\alpha)}(R_H, t) \phi_{j_D}^{(\alpha)}(R_D, t), \quad (11)$$

which is an expansion represented by Hartree products on the time-dependent basis functions $\phi_k^{(\alpha)}(R_k, t)$, where α corresponds to the electronic state and with $k = \{H, D\}$. Dynamics calculations obtained below are performed by setting $n_H = n_D = 12$ in a uniform grid with $N_H = N_D = 101$ grid points for each coordinate on the interval $0.5a_0 < q < 6.0a_0$. Photodissociation probabilities are computed through the wave packet flux absorbed by a complex absorbing potential (CAP) located in each coordinate at $R_H = R_D = 5.5a_0$. The 2D vibrational ground state of \tilde{X}^1A_1 electronic state is computed inside the MCTDH package via propagation in imaginary time.³⁹

III. RESULTS

A. Local excitation of O-H and O-D molecular modes

To control the photodissociation with an IR-pump-UV-dump laser pulse of the isotopomer HOD, the first step is to analyze the vibrational excited states of the electronic ground state. Figure 4 shows the three lowest vibrational states of the electronic ground

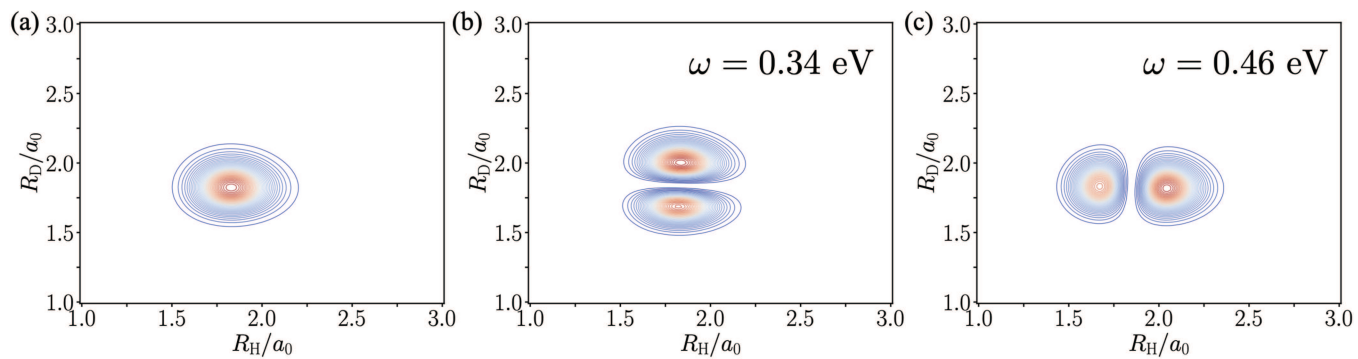


FIG. 4. Probability density of the three lowest vibrational states of semi-heavy water molecule in the ground electronic state. (a) Vibrational ground state. (b) First vibrational excited state which represents the excitation of R_D mode at frequency $\omega_{IR} = 0.34$ eV. (c) Second vibrational excited that corresponds to the excitation of R_H mode at frequency $\omega_{IR} = 0.46$ eV. The excited states seem as two independent orthogonal harmonic oscillators, the first along R_D bond coordinate and the second in the R_H direction.

state for semi-heavy water molecule with its corresponding excitation energy with respect to the vibrational ground state in Fig. 4(a). The first and second excited vibrational states represent the excitation of the OD and OH bond lengths and are shown in Figs. 4(b) and 4(c), respectively. Note that these excited vibrational states differ in around 0.12 eV, which facilitates to activate each mode independently with an IR ultrashort laser pulse due to the difference of masses, in contrast to H_2O molecule where the energy difference between symmetric and asymmetric mode is in the order of 0.012 eV^{40,41} and laser bandwidth can overlap with both normal modes. Exciting a local mode can achieve control over dissociation by pumping with an IR laser, which creates an excited vibrational wave packet. OH bond length is excited with an IR pulse that has a carrier frequency $\omega_{IR} = 0.46$ eV and a polarization parallel to the x -axis ($\theta = 0^\circ$), which results in the mean bond distance dynamics shown in Fig. 5(a). This IR-excitation is performed to prepare the wavepacket in the electronic ground state \tilde{X}^1A_1 until a given time at which the $\langle R_H \rangle$ coordinate has the maximum length with a given positive momentum. This time corresponds to $t \approx 61.0$ fs. For OD bond length excitation, the IR laser pulse has a carrier frequency $\omega_{IR} = 0.34$ eV and a polarization parallel to the y -axis [$\theta = 90^\circ$ in Eq. (6)]. Similarly, this second wave packet preparation has the maximum value of $\langle R_D \rangle$ with positive momentum at $t \approx 68.0$ fs [see Fig. 5(b)]. We point out that the UV laser pulse is applied around two femtoseconds before these times to conserve the positive momentum during the UV-laser-pulse duration. The results of the mean bond distance dynamics for datasets B and C are shown in Appendix B.

B. Photodissociation dynamics by IR+UV laser pulses

The control over dissociation can be achieved by exciting a local mode by pumping with an IR laser, which creates an excited vibrational wavepacket prior to the UV electronic excitation, that occurs at a well selected time delay. Hence, for the case of $HOD \rightarrow H + OD$ control scheme, the UV laser pulse has a time delay $\tau = 19.0$ fs and a pulse time duration $T = 3.0$ fs. We consider five different carrier frequencies in the interval $\omega_{UV} = [8.0, 10.0]$ eV, where the resonant

frequency at equilibrium position is $\omega = V_E(R_0, R_0) - V_G(R_0, R_0) = 9.27$ eV. The UV laser pulse transfers the population to the excited electronic state \tilde{A}^1B_1 from the excited vibrational wave packet in the ground electronic state generated by the IR laser pulse. The function of the time delay between the IR and UV pulses is to shift the initial position of the wave packet from the saddle point in the excited electronic state, which leads to a dissociative photodynamics over the selected bond coordinate. The mechanism is slightly independent of the reduced mass difference of hydrogen and deuterium atoms because IR laser pulse polarization and vibrational excited energy difference allow exciting a specific local mode of semi-heavy water molecules.

Figure 6(a) shows the dissociation probabilities of the R_H bond as a function of time for different carrier laser frequencies ω_{UV} . We observe notable differences as a function of UV carrier frequency, where the maximum value appears for $\omega_{UV} = 8.5$ eV and the minimum for $\omega_{UV} = 10.0$ eV. The maximum dissociation probability occurs because the carrier laser frequency equal to 8.5 eV is the closest value to the resonant frequency ($\omega = V_E - V_G = 8.7$ eV) between the two electronic states at $R_H \approx 2.0a_0$ and R_D at equilibrium. These positions consider that wavepacket moves along R_H coordinate and remains almost constant in coordinate R_D , and $R_H \approx 2.0a_0$ corresponds to the mean position of the wavepacket at which the UV-laser pulse drives the molecule [see Fig. 5(a)]. Hence, the Franck-Condon region overlaps with the center of the UV laser pulse spectrum, where the effective transition strength is generally maximum. On the contrary, $\omega_{UV} = 10.0$ eV has the largest detuning with a value of ~ 1.27 eV. Thus, a small portion of the UV laser pulse spectrum (FWHM ≈ 2.7 eV) overlaps with the Franck-Condon region, which decreases the effective transition strength, and as a consequence, population transfer reduces.

Dissociation control over the R_D bond coordinate is generally a challenge at the experimental level due to the reduced mass difference between OH and OD modes. Photodissociation probabilities for the R_D bond in the order of the R_H bond can be obtained if the time delay of the UV laser pulse is selected suitably with a great precision, as Fig. 6(b) shows. Similar to R_H dissociation

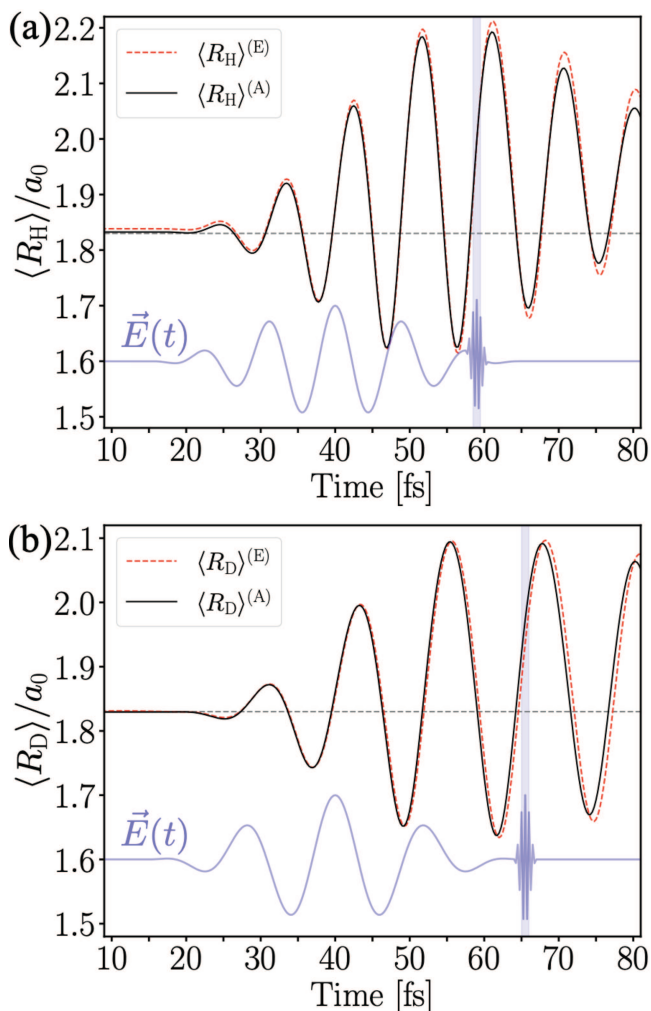


FIG. 5. Average position for bond coordinates of HOD molecule under IR-excitation. (a) Mean bond distance as a function of time for R_H coordinate pumped with a IR laser pulse parallel to the x -axis. (b) Mean bond distance as a function of time for R_D coordinate pumped with a IR laser pulse parallel to the y -axis. Laser pulse parameters in each case are given in Table I. In all panels, the exact calculation of $\langle R_k \rangle^{(E)}$ is compared with the mean bond distance $\langle R_k \rangle^{(A)}$ that results of the calculation with ML-PES from dataset A. The purple line corresponds to the IR-UV combined laser pulse in Eq. (6) and shaded regions represent the time interval at which the UV laser is applied.

control, the maximum dissociation probability for the D+OH channel occurs at $\omega_{UV} = 9.0$ eV and the minimum is maintained at $\omega_{UV} = 10.0$ eV. In this case, the maximum dissociation probability occurs because the carrier laser frequency equal to 9.0 eV is almost equal to the resonant frequency ($\omega = V_E - V_G = 9.03$ eV) between the two electronic states at $R_D \approx 1.9a_0$ and R_H at equilibrium. Now, we consider that wavepacket moves along R_D coordinate and stays almost constant in coordinate R_H , and $R_D \approx 1.9a_0$ refers to the point at which the UV-laser pulse drives the molecule [see Fig. 5(b)].

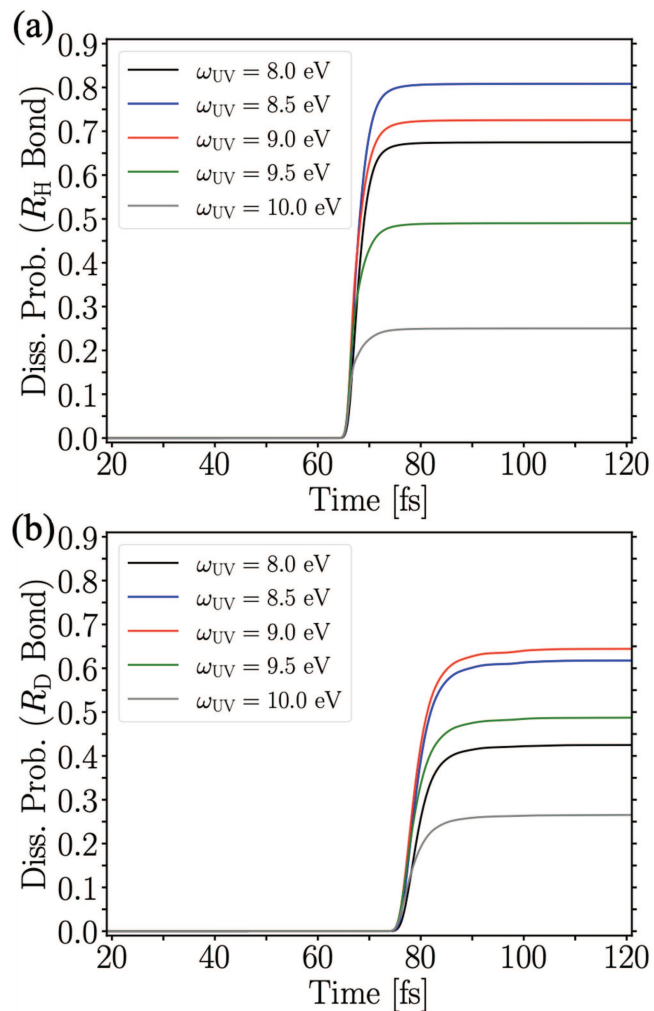


FIG. 6. Photodissociation probabilities for different UV laser frequencies. Photodissociation probabilities for dissociating channels (a) H+OD and (b) D+OH when the HOD molecule is excited with an infrared laser pulse polarized along the x -axis and y -axis, respectively.

C. Statistical implications of ML-PES

1. Vibrational ground state

The first expectation value to analyze is the vibrational ground state in the \tilde{X}^1A_1 electronic potential. We point out that any small change in the initial state can significantly modify the dynamics of the system due to the non-linear behavior of potential energy surfaces. Hence, it is fundamental to keep the initial state as accurate as possible to avoid propagation errors since $t = 0$.

The values of the vibrational ground state energy for all datasets are shown in Table III. As it is expected, the minimum error for ML-PES corresponds to dataset C, which is the most accurate for the electronic ground state potential. With an estimated difference

TABLE III. Initial state energy. Values of the initial state energy for the three datasets used to generate ML-PES with their corresponding absolute percentage error. The exact initial state energy is taken as reference in $E_0 = 0.0$. Energy values are in meV.

	Datasets			2D-spline
	A	B	C	
E_0 (meV)	-7.32	-6.59	0.86	0.07
Error (%)	1.78	1.61	0.21	0.02

of around 8.7×10^{-4} eV with respect to the exact calculation. These results are within the accepted experimental errors.⁴² However, note that a standard interpolation methodology (a 2D spline interpolation) with dataset A has better accuracy than ML-PES with larger datasets, which suggests that even advanced machine learning techniques could lead to less accurate representations of potential energy surfaces. Hence, ML-PES of the electronic ground state generated with datasets A and B with a difference of >6.2 meV should be used carefully in dynamics calculations, despite their MAPE values.

2. Mean bond distance

The second step to control the dissociation process in the semi-heavy water molecule is to excite one of the local modes from the vibrational ground state with an IR laser pulse. A comparison of the mean bond distance obtained with ML-PES is shown in Fig. 5. We observe minimum differences for $\langle R_H \rangle$ and $\langle R_D \rangle$, i.e., the calculations with ML-PES^(A) (solid-black line) are underestimated and differ from the numerical exact calculation (red-dashed line) at long times. This is due to the small deviations of the ML-PES with the exact PES as bond distance coordinates increase, as Fig. 2(a) shows, which give rise to a total mean absolute percentage error of 0.5% and 0.8% for R_H and R_D bond distances, respectively.

It is worth noting that differences are notorious at long times ($t > 50$ fs), which is because the wave packet completes a few oscillations along the ML-PES accumulating errors. For example, in the case of IR-excitation of R_D mode, the MAPE for the first 50 fs is 0.1%, while for the next 50 fs (time interval $t = [50 - 100]$ fs), the error increases up to 1.6%. Hence, we point out that accurate ML-PES with small errors support a wave function propagation in a few dozen femtoseconds at the electronic ground state energy level, in contrast to long propagation times.

Calculations of $\langle R_H \rangle$ and $\langle \hat{R}_H \rangle$ with ML-PES^(B) and ML-PES^(C) results in a MAPE that can be considered negligible, and no relevant differences are observed in the dynamics.

3. Photodissociation mechanism: Effects of excited ML-PES

Figure 7(a) shows the comparison of dissociation probabilities of R_H bond as a function of time for UV carrier laser frequencies $\omega_{UV} = 9.0$ and 10.0 eV, which are opposite in terms of the mean absolute percentage error. The differences in the calculations with ML-PES appear before stabilization and are maintained after the

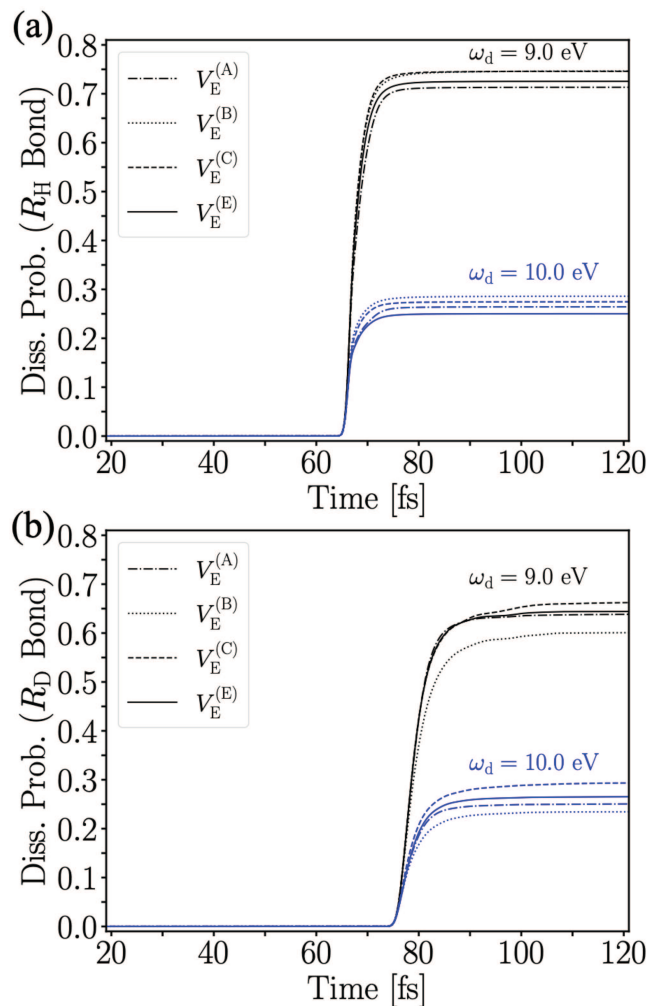


FIG. 7. Comparison of photodissociation probabilities calculated with ML-PES for different UV laser frequencies. Photodissociation probabilities for dissociating channels (a) $H+OD$ and (b) $D+OH$ when the HOD molecule is excited with an infrared laser pulse polarized along the x-axis and y-axis, respectively.

stabilization of dissociation probability. For comparison, dissociation probabilities calculated in photodynamics with ML-PES can differ by up to 5% in comparison with the exact calculation, both for $\omega_{UV} = 9.0$ eV and 10.0 eV. The mean absolute percentage errors are given in Table IV for all UV laser frequencies. We notice that the highest error corresponds to $\omega_{UV} = 10$ eV and the lowest to $\omega_{UV} = 8.5 - 9.0$ eV. The latter is due to the laser frequency being detuned with respect to the resonance frequency between the two electronic states and as a consequence, the density of vibrational states in the \tilde{A}^1B_1 electronic state that participates in population transfer from the electronic ground state is higher than the resonance scenario ($\omega_{UV} \sim 8.5 - 9.0$ eV), i.e., predicted energy points of

TABLE IV. Mean absolute percentage errors of photodissociation probabilities. Error of photodissociation probabilities of R_H and R_D bonds calculated using ML-PES predicted with datasets A, B, C and for the PES fitted using a 2D-spline interpolation.

		Driving frequency (ω_d)				
Mode	Dataset	8.0 eV	8.5 eV	9.0 eV	9.5 eV	10.0 eV
R_H	A	7.95%	2.56%	2.89%	8.62%	14.34%
	B	2.55%	2.76%	1.67%	1.44%	5.66%
	C	4.61%	0.79%	2.84%	6.48%	9.80%
	2D-spline	0.37%	0.11%	0.16%	0.27%	0.14%
R_D	A	10.01%	3.62%	0.85%	3.88%	5.52%
	B	2.56%	2.60%	6.66%	9.62%	11.60%
	C	3.30%	0.23%	2.88%	6.45%	10.61%
	2D-spline	0.96%	0.12%	0.34%	0.51%	0.57%

the repulsive energy region influence the photodynamics, which is a predicted energy region with small accuracy as the shaded regions in Figs. 3(d)–3(f) illustrate.

Similar differences are found in the photodissociation probabilities for the D+OH channel, with the largest MAPE for the detuned case being $\omega_{UV} = 10.0$ eV [see Fig. 7(b)]. We point out that the errors depend on the precision in the ML-PES region where the wave packet moves. For example, for dynamics calculations with ML-PES^(B) by selecting the R_D bond as the bond-breaking goal, the error tends to increase as the UV laser frequency increases (see Table IV). However, other cases have the minimum at the smallest detuning ($\omega_d = 9.0$ eV), and the MAPE increases as detuning increases. The latter confirms that small variations in high-energy regions of ML-PES can lead to photodissociation probabilities with errors larger than 6%. Results shown in Table IV agree with the differences of the highest energy regions in Fig. 3 (shaded regions) with respect to the exact PES, which are the regions with the largest errors point by point. Photodissociation probabilities for laser frequencies $\omega_d = 8.0$, 8.5, and 9.5 eV for all datasets are shown in Appendix C.

IV. DISCUSSIONS AND CONCLUSIONS

We have studied the machine-learning potential energy surface implications in photodynamics calculations that lead to bond-breaking mechanisms in the H+OD and D+OH dissociation channels of semi-heavy water molecules, comparing ML-PES dynamics calculations with analytical-PES photodynamics. In the context of machine-learning predictions, our work reveals significant differences between the two scenarios, which establishes significant key aspects highlighting both the robustness and limitations of ML-PES in molecular dynamics calculations. We show that the observed discrepancies in photodynamics calculations with ML-PES in the vibrational ground state energy, mean bond distance, and dissociation probability depend on specific regions of the potential energy surface and laser parameters. Although ML-dynamics calculations show accurate results for the largest dataset, a conventional

multidimensional spline interpolation^{43,44} with the size of dataset A can be more accurate and requires less computational resources.

The results for the electronic ground state \tilde{X}^1A_1 show a high accuracy for all ML models implemented, which is demonstrated by the small errors found in the vibrational ground state energy and mean bond distances. We highlight the results with dataset A because of their reduced number of data points. Hence, despite the challenges in molecular dynamics, we show in Sec. III C that ground state dynamics performed with ML-PES have great accuracy. For the mean bond distance scenario, good precision is kept in the context of ultrafast molecular dynamics. The latter is due to the wave packet propagation time being insufficient to accumulate errors generated by small perturbations along ML-PES. For example, the mean absolute percentage error of photodynamics calculations for $t > 50$ fs increases up to one order of magnitude in comparison with propagation times smaller than 50 fs.

On the contrary, independent of the size of the dataset, the accuracy of the ML-PES for excited state \tilde{A}^1B_1 is reduced due to the dissociative character of this electronic state and high-energy regions involved in the photodynamics. The latter is reflected in photodissociation probabilities errors in Table IV. The nature of \tilde{A}^1B_1 state makes it highly complex with non-linearities, which usually is difficult to converge and can lead to overfitting with small datasets. In contrast, a standard spline interpolation can be more efficient with small datasets, as Table IV shows for photodissociation probabilities of R_H and R_D bonds. However, we point out that our implemented ML model avoids overfitting in predicting energy points. We highlight the limitations of ML training models to accurately generalize patterns from datasets of multidimensional electronic states with a small sampling in the repulsive and dissociative energy regions, even considering the symmetry of the electronic states for the HOD and water molecules that could simplify ML models and improve their precision. This issue represents one of the challenges in the context of machine-learning techniques applied in molecular dynamics because, in general, it requires a huge amount of data points to capture the multimode high-energy regions that dominate defined molecular processes. The computational efforts to add points into the dataset by performing additional *ab initio* calculations reduce the gain desired in computational resources by implementing ML techniques to reproduce correctly the complete PESs. Hence, other promising approaches like physics-informed neural networks (PINNs)⁴⁵ or hybrid methods that combine data-driven learning with known physical laws, such as multiple instant learning⁴⁶ can be applied in the future to enhance the accuracy in multidimensional multistate photodynamics calculations that involve high-energy regions by implementing machine-learning techniques.

Our work demonstrated the viability of generating ML-PES from small datasets in molecular dynamics simulations in the Franck–Condon region of the electronic ground state^{17,47} and contributes to the development of MD simulations aided by ML techniques,⁴⁸ which is fundamental for studying light–matter interactions,^{49–51} cavity-QED,^{52,53} and chemical reaction control.⁵⁴ Further, the results show that photodynamics calculations with ML-PES governed mainly by non-linearities should be interpreted carefully because their nature make it difficult to reach convergence with conventional ML techniques with standard *ab initio* data sets.

Extensions of this work could open further possibilities for developing novel hybrid and efficient techniques in molecular dynamics simulations and contribute to the ML technique selection to be introduced in multidimensional molecular dynamics according to the phenomenon under study.

ACKNOWLEDGMENTS

J.d.l.C. and J.F.T. are supported by ANID-Fondecyt Iniciación No. 11230679. We also thank “Núcleo de Investigación No. 7 UCN-VRIDT 076/2020, Núcleo de modelación y simulación científica (NMSC).”

AUTHOR DECLARATIONS

Conflict of Interest

The authors have no conflicts to disclose.

Author Contributions

Joaquin de la Cerdá: Supervision (equal); Validation (equal). **Johan F. Triana:** Conceptualization (equal); Formal analysis (equal); Funding acquisition (equal); Methodology (equal); Project administration (equal); Supervision (equal); Validation (equal); Visualization (equal); Writing – original draft (equal); Writing – review & editing (equal).

DATA AVAILABILITY

The data that support the findings of this study are available within the article.

APPENDIX A: DATASETS GRID POINTS

The basic grid of points for each dataset at which electronic state energies are calculated as defined by the following values of $R_H = R_D$ in units of Bohr radius a_0 :

- Dataset A: $R_H = R_D = 0.8, 1.0, 1.2, 1.3, 1.4, 1.5, 1.6, 1.7, 1.8, 1.9, 2.0, 2.1, 2.2, 2.3, 2.4, 2.5, 3.0, 3.5, 4.0, 4.5, 5.0, 5.5, 6.0$.
- Dataset B: $R_H = R_D = 0.8, 0.9, 1.0, 1.1, 1.2, 1.3, 1.4, 1.5, 1.6, 1.7, 1.8, 1.9, 2.0, 2.1, 2.2, 2.3, 2.4, 2.5, 2.75, 3.0, 3.25, 3.5, 3.75, 4.0, 4.25, 4.5, 4.75, 5.0, 5.25, 5.5, 5.75, 6.0$.
- Dataset C: $R_H = R_D = 0.8, 0.9, 1.0, 1.1, 1.2, 1.3, 1.35, 1.4, 1.45, 1.5, 1.55, 1.6, 1.65, 1.7, 1.75, 1.8, 1.85, 1.9, 1.95, 2.0, 2.05, 2.1, 2.15, 2.2, 2.25, 2.3, 2.35, 2.4, 2.5, 2.75, 3.0, 3.25, 3.5, 3.75, 4.0, 4.25, 4.5, 4.75, 5.0, 5.25, 5.5, 5.75, 6.0$.

APPENDIX B: MEAN BOND LENGTH

The mean bond distance dynamics for OH bonds calculated by implementing ML-PES fitted with data sets B and C are shown in Fig. 8(a). Similarly, Fig. 8(b) shows the dynamics for $\langle R_D \rangle$.

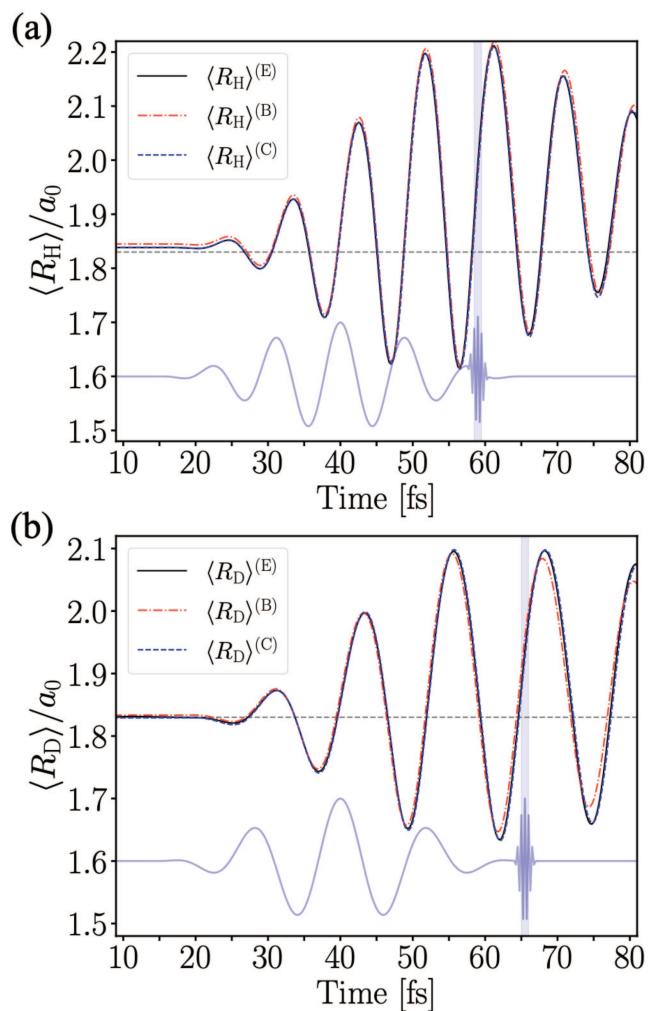


FIG. 8. Average position for bond coordinates of the HOD molecule under IR-excitation. (a) Mean bond distance as a function of time for R_H coordinate pumped with a IR laser pulse parallel to the x-axis. (b) Mean bond distance as a function of time for R_D coordinate pumped with a IR laser pulse parallel to the y-axis. Laser pulse parameters in each case are given in Table I. In all panels, the exact calculation of $\langle R_k \rangle^{(E)}$ is compared with the mean bond distance that results in the calculation of ML-PES from dataset B ($\langle R_k \rangle^{(B)}$) and dataset C ($\langle R_k \rangle^{(C)}$). The purple line corresponds to the IR-UV combined laser pulse in Eq. (6), and shaded regions represent the time interval at which UV laser is applied.

APPENDIX C: DISSOCIATION PROBABILITIES

Figure 9(a) shows the comparison of dissociation probabilities of the OH bond as a function of time for UV carrier laser frequencies $\omega_{UV} = 8.0, 8.5$, and 9.5 eV. Similarly, Fig. 9(b) shows the comparison of the OD bond.

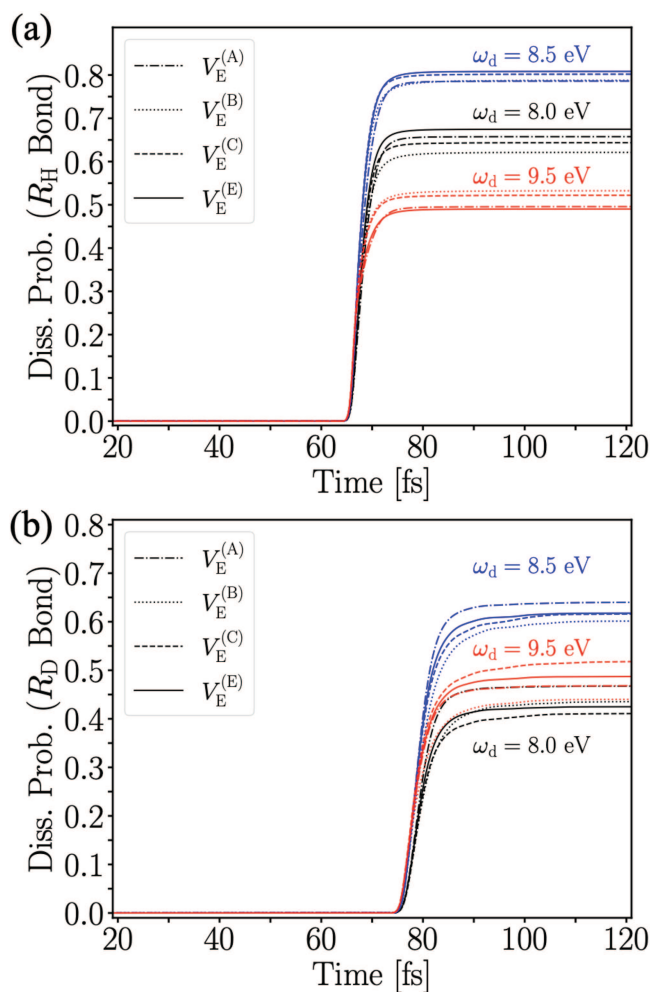


FIG. 9. Comparison of photodissociation probabilities calculated with ML-PES for different UV laser frequencies. Photodissociation probabilities for dissociating channels (a) H+OD and (b) D+OH when the HOD molecule is excited with an infrared laser pulse polarized along the x-axis and y-axis, respectively.

REFERENCES

- 1 V. Engel, R. Schinke, and V. Staemmler, *J. Chem. Phys.* **88**, 129 (1988).
- 2 S. Meyer and V. Engel, *J. Phys. Chem. A* **101**, 7749 (1997).
- 3 R. Prosmitti, A. A. Buchachenko, P. Villarreal, and G. Delgado-Barrio, *Theor. Chem. Acc.* **106**, 426 (2001).
- 4 D. Xie, Y. Lu, D. Xu, and G. Yan, *Chem. Phys.* **270**, 415 (2001).
- 5 X. Huang, B. J. Braams, J. M. Bowman, R. E. A. Kelly, J. Tennyson, G. C. Groenenboom, and A. van der Avoird, *J. Chem. Phys.* **128**, 034312 (2008).
- 6 B. F. E. Curchod, I. Tavernelli, and U. Rothlisberger, *Phys. Chem. Chem. Phys.* **13**, 3231 (2011).
- 7 T. Tsutsumi, Y. Harabuchi, R. Yamamoto, S. Maeda, and T. Taketsugu, *Chem. Phys.* **515**, 564 (2018).
- 8 S. Gómez, E. Spinlove, and G. Worth, *Phys. Chem. Chem. Phys.* **26**, 1829 (2024).
- 9 F. Noé, A. Tkatchenko, K.-R. Müller, and C. Clementi, *Annu. Rev. Phys. Chem.* **71**, 361 (2020).
- 10 Q. Tong, P. Gao, H. Liu, Y. Xie, J. Lv, Y. Wang, and J. Zhao, *J. Phys. Chem. Lett.* **11**, 8710 (2020).
- 11 M. Pinheiro, F. Ge, N. Ferré, P. O. Dral, and M. Barbatti, *Chem. Sci.* **12**, 14396 (2021).
- 12 J. U. Song, K. Choi, S. M. Oh, and B. Kahng, *Chaos* **33**, 073148 (2023).
- 13 J. Behler and M. Parrinello, *Phys. Rev. Lett.* **98**, 146401 (2007).
- 14 J. Behler, *Int. J. Quantum Chem.* **115**, 1032 (2015).
- 15 K. Gubaev, E. V. Podryabinkin, and A. V. Shapeev, *J. Chem. Phys.* **148**, 241727 (2018).
- 16 M. Rupp, A. Tkatchenko, K.-R. Müller, and O. A. von Lilienfeld, *Phys. Rev. Lett.* **108**, 058301 (2012).
- 17 M. J. M. de Oca-Estévez, Á. Valdés, D. Koner, T. González-Lezana, and R. Prosmitti, *Chem. Phys. Lett.* **856**, 141641 (2024).
- 18 F. A. Faber, L. Hutchison, B. Huang, J. Gilmer, S. Schoenholz, G. E. Dahl, O. Vinyals, S. Kearnes, P. F. Riley, and O. A. von Lilienfeld, *J. Chem. Theory Comput.* **13**, 5255 (2017).
- 19 Y. Guan, H. Guo, and D. R. Yarkony, *J. Chem. Theory Comput.* **16**, 302 (2020).
- 20 J. O. Richardson, *J. Chem. Phys.* **158**, 011102 (2023).
- 21 P. O. Dral, M. Barbatti, and W. Thiel, *J. Phys. Chem. Lett.* **9**, 5660 (2018).
- 22 D. Hu, Y. Xie, X. Li, L. Li, and Z. Lan, *J. Phys. Chem. Lett.* **9**, 2725 (2018).
- 23 G. W. Richings and S. Habershon, *Acc. Chem. Res.* **55**, 209 (2022).
- 24 Y. Guan, B. Fu, and D. H. Zhang, *J. Chem. Phys.* **147**, 224307 (2017).
- 25 J. Westermayr and P. Marquetand, *Chem. Rev.* **121**, 9873 (2021).
- 26 D. Hu and P. Huo, *J. Chem. Theory Comput.* **19**, 2353 (2023).
- 27 M. Kowalewski, K. Bennett, and S. Mukamel, *J. Chem. Phys.* **144**, 054309 (2016).
- 28 J. F. Triana, F. J. Hernández, and F. Herrera, *J. Chem. Phys.* **152**, 234111 (2020).
- 29 B. Jiang, J. Li, and H. Guo, *J. Phys. Chem. Lett.* **11**, 5120 (2020).
- 30 A. Kushwaha and T. J. Dhilip Kumar, *Int. J. Quantum Chem.* **123**, e27007 (2023).
- 31 J. Zhang, D. G. Imre, and J. H. Frederick, *J. Phys. Chem.* **93**, 1840 (1989).
- 32 N. Elghobashi, P. Krause, J. Manz, and M. Oppel, *Phys. Chem. Chem. Phys.* **5**, 4806 (2003).
- 33 J. F. Triana, D. Peláez, M. Hochlaf, and J. L. Sanz-Vicario, *Phys. Chem. Chem. Phys.* **24**, 14072 (2022).
- 34 D. Schleier, J. Kamer, A. Jiao, G. F. Schneider, H. Linnartz, and J. Bouwman, *Phys. Chem. Chem. Phys.* **26**, 15547 (2024).
- 35 F. Chollet *et al.*, see <https://keras.io> for “Keras” (2015).
- 36 M. Beck, A. Jäckle, G. Worth, and H.-D. Meyer, *Phys. Rep.* **324**, 1 (2000).
- 37 G. Worth, M. Beck, A. Jäckle, and H. Meyer, see <http://mctdh.uni-hd.de> for “The MCTDH Package, Version 8.4” (2007).
- 38 H. Meyer, F. Gatti, and G. Worth, *Multidimensional Quantum Dynamics: MCTDH Theory and Applications* (John Wiley & Sons, 2009).
- 39 H.-D. Meyer and G. A. Worth, *Theor. Chem. Acc.* **109**, 251 (2003).
- 40 M. H. Brooker, G. Hancock, B. C. Rice, and J. Shapter, *J. Raman Spectrosc.* **20**, 683 (1989).
- 41 A. A. Kananenka and J. L. Skinner, *J. Chem. Phys.* **148**, 244107 (2018).
- 42 J. Chalmers and P. Griffiths, *Handbook of Vibrational Spectroscopy*, 5 Volume Set (Wiley, 2002).
- 43 I. J. Schoenberg, *Quart. Appl. Math.* **4**, 45–99 and 112–141 (1946).
- 44 R. Burden, J. Faires, and A. Burden, *Numerical Analysis* (Cengage Learning, 2015).
- 45 A. Zafra, E. L. Gibaja, and S. Ventura, *Appl. Soft Comput.* **11**, 93 (2011).
- 46 M. Raissi, P. Perdikaris, and G. Karniadakis, *J. Comput. Phys.* **378**, 686 (2019).
- 47 M. J. Montes de Oca-Estévez, Á. Valdés, and R. Prosmitti, *Phys. Chem. Chem. Phys.* **26**, 7060 (2024).
- 48 X. Li, N. Lubbers, S. Tretiak, K. Barros, and Y. Zhang, *J. Chem. Theory Comput.* **20**, 891 (2024).
- 49 I.-C. Benea-Chelmus, F. F. Settembrini, G. Scalari, and J. Faist, *Nature* **568**, 202 (2019).
- 50 F. Charfeddine, A. Zanchet, O. Yazidi, C. A. Cuevas, A. Saiz-Lopez, L. Bañares, and A. García-Vela, *J. Chem. Phys.* **160**, 074301 (2024).
- 51 P. Recio, R. Y. Bello, G. A. García, A. Zanchet, J. González-Vázquez, L. Bañares, and S. Marggi Poullain, *Phys. Chem. Chem. Phys.* **26**, 21441 (2024).
- 52 F. Herrera and J. Owrusky, *J. Chem. Phys.* **152**, 100902 (2020).
- 53 J. F. Triana and F. Herrera, *New J. Phys.* **24**, 023008 (2022).
- 54 W. Ahn, J. F. Triana, F. Recabal, F. Herrera, and B. S. Simpkins, *Science* **380**, 1165 (2023).